Supplemental Material for *Scaling laws in supply limited Aeolian sand transport*

Sandesh Kamath[1], Yaping Shao[1], Eric J. R. Parteli[2]

[1]Institute of Geophysics and Meteorology, University of Cologne, Germany
[2]Faculty of Physics, University of Duisburg-Essen, Germany

Corresponding author: Sandesh Kamath, skamath@uni-koeln.de

Abstract

In this Supplemental Material, we briefly review the features of the Discrete-Element-Method referred to in the main document, including the complete set of the equations of motion, the details of the numerical integration of these equations, and the models of particle-particle interactions adopted in the simulations of Aeolian sand transport. Furthermore, we present the results of our numerical simulations performed to verify our model, the vertical profiles of the wind velocity and grain-borne shear stress during steady-state transport, and the behavior of the transport layer thickness as a function of the thickness of mobile sand layer, as mentioned in the main document.

1 Discrete-Element-Method

In the Discrete-Element-Method, the equations of motion are solved for every particle in the system under consideration of the main forces acting on them. These forces are, in the process of non-suspended Aeolian transport of cohesionless particles, the drag force, the inter-particle contact forces and the gravitational force.

1.1 Equations of motion and contact force model for the sand particles

The equation of translational motion for a particle of mass m_i at position $\mathbf{r}_i$ reads,

$$m_i \ddot{\mathbf{r}}_i = \mathbf{F}_i^{\mathrm{d}} + m_i \mathbf{g} + \sum_{\substack{1 \le j \le N_{\mathrm{p}} \\ j \neq i}} \mathbf{F}_{ij}^{\mathrm{c}} \tag{1}$$

where $\mathbf{F}_i^{\mathrm{d}}$ is the drag force on particle i, computed with the model described in the main document, $\mathbf{g}$ is gravity, N_{p} is the number of particles in the system, j denotes the index of a neighbouring particle that is in contact with particle i, and $\mathbf{F}_{ij}^{\mathrm{c}}$ denotes the contact force exerted by particle j on i (with $\mathbf{F}_{ij}^{\mathrm{c}} = -\mathbf{F}_{ji}^{\mathrm{c}}$).

Contact between particles j and i occurs with their center-to-center distance is smaller than the sum of their radii, i.e., the contact force acts only if the particles overlap. To model the contact force, the following equation is used to define the overlap,

$$\delta_{ij,\mathrm{n}} = \min\left\{0, \frac{1}{2}\left[d_i + d_j\right] - \left(\mathbf{r}_i - \mathbf{r}_j\right) \cdot \mathbf{e}_{ij,\mathrm{n}}\right\} \tag{2}$$

where d_i and d_j are the diameters of particles i and j, respectively, $\mathbf{r}_{ij} = \mathbf{r}_i - \mathbf{r}_j$, with $\boldsymbol{r}_j$ standing for the position of particle j, and $\mathbf{e}_{ij,\mathrm{n}} = \mathbf{r}_{ij}/r_{ij}$ denotes the normal unit vector pointing from the center of particle j to the center of particle i, with $r_{ij} = |\mathbf{r}_{ij}|$.

There are various contact force models for application in DEM simulations, and the modelling of these forces is still an active matter of research (Cundall & Strack, 1979; Schäfer et al., 1996; Brilliantov et al., 1996; Silbert et al., 2001; Di Renzo & Di Maio, 2004; Pöschel & Schwager, 2005; Kruggel-Emden et al., 2007; Luding, 2008; Machado et al., 2012; Parteli et al., 2014; Fan et al., 2017; Schmidt et al., 2020; Santos et al., 2020). In our simulations, we adopt the linear spring-dashpot model, because this model has been employed in previous simulations of wind-blown sand that reproduced the scaling laws associated with Aeolian transport over fully erodible beds (Carneiro et al., 2011, 2013; Durán et al., 2012; Comola et al., 2019).

Specifically, $\mathbf{F}_{ij}^{\mathrm{c}}$ can be described as the sum of a normal component, $\mathbf{F}_{ij,\mathrm{n}}^{\mathrm{c}}$, and a tangential component, $\mathbf{F}_{ij,\mathrm{t}}^{\mathrm{c}}$. Each of these components encodes an elastic term and a dissipative term, while the magnitude of the tangential force is bounded by the Coulomb friction criterion. The equations for $\mathbf{F}_{ij,\mathrm{n}}^{\mathrm{c}}$ and $\mathbf{F}_{ij,\mathrm{t}}^{\mathrm{c}}$ read (Cundall & Strack, 1979; Silbert et al., 2001; Santos

et al., 2020)

$$\mathbf{F}^{\mathrm{c}}_{ij,\mathrm{n}} = k_{\mathrm{n}}\delta_{ij,\mathrm{n}}\mathbf{e}_{ij,\mathrm{n}} - \gamma_{\mathrm{n}}m_{\mathrm{eff}}\mathbf{v}_{ij,\mathrm{n}} \tag{3}$$

$$\mathbf{F}^{\mathrm{c}}_{ij,\mathrm{t}} = -\min\left\{\mu_{\mathrm{s}}|\mathbf{F}^{\mathrm{c}}_{ij,\mathrm{n}}|, k_{\mathrm{t}}\xi_{ij,\mathrm{t}} + \gamma_{\mathrm{t}}m_{\mathrm{eff}}|\mathbf{v}_{ij,\mathrm{t}}|\right\}\frac{\mathbf{v}_{ij,\mathrm{t}}}{|\mathbf{v}_{ij,\mathrm{t}}|} \tag{4}$$

where $m_{\mathrm{eff}} = m_i m_j/(m_i + m_j)$, with m_i and m_j denoting the masses of particles i and j, respectively, k_{n}, k_{t}, γ_{n}, γ_{t} and μ_{s} are model parameters, discussed in Section 1.3 below, while the relative normal velocity $\mathbf{v}_{ij,\mathrm{n}}$ and the relative tangential velocity $\mathbf{v}_{ij,\mathrm{t}}$ between particles i and j are computed via

$$\mathbf{v}_{ij,\mathrm{n}} = (\mathbf{v}_{ij}\cdot\mathbf{e}_{ij,\mathrm{n}})\mathbf{e}_{ij,\mathrm{n}} \tag{5}$$

$$\mathbf{v}_{ij,\mathrm{t}} = \mathbf{v}_{ij} - \mathbf{v}_{ij,\mathrm{n}} - \frac{1}{2}(\boldsymbol{\omega}_i + \boldsymbol{\omega}_j)\times(\mathbf{r}_i - \mathbf{r}_j) \tag{6}$$

with $\mathbf{v}_{ij} = \mathbf{v}_i - \mathbf{v}_j$ denoting the difference between the velocities of particles i and j ($\mathbf{v}_i$ and $\mathbf{v}_j$, respectively), and $\boldsymbol{\omega}_i$ and $\boldsymbol{\omega}_j$ standing for their respective rotational velocities. Moreover, in Eq. (4), $\xi_{ij,\mathrm{t}}$ is the tangential displacement accumulated as the particles are in contact. The displacement is set as zero at initiation of the contact and is computed in the reference frame of the rotating particle pair to compensate for the effect of rigid body rotations, as described in detail in previous work (Silbert et al., 2001; Santos et al., 2020).

The equation of rotational motion for particle i reads

$$I_i\boldsymbol{\omega}_i = \sum_{\substack{1\le j\le N_{\mathrm{p}}\\ j\neq i}}\mathbf{M}_{ij} \tag{7}$$

with $I_i = m_i d_i^2/10$ and $\boldsymbol{\omega}_i$ denoting the moment of inertia and the angular velocity of particle i, respectively, and $\mathbf{M}_{ij}$ corresponding to the torque on particle i associated with $\mathbf{F}^{\mathrm{c}}_{ij,\mathrm{t}}$.

1.2 Contact forces between mobile and rigid particles (non-erodible elements)

The contact forces between mobile sand particles and the rigid particles constituting the roughness elements of the bed are computed using the same model as in the previous section, but considering that the rigid particles have an infinite mass (Verbücheln et al., 2015). Specifically, the normal and tangential components of the contact force from a rigid particle j on a mobile particle i are computed with Eqs. (3) and (4), respectively, by setting $m_{\mathrm{eff}} = m_i$. Furthermore, contact forces between rigid particles are not considered.

1.3 Model parameters

Table 1 displays the values of the parameters in Eqs. (3) and (4), i.e., the elastic constants k_{n} and k_{t}, the damping coefficients γ_{n} and γ_{t}, and the Coulomb friction coefficient, μ_{s}. The elastic and damping constants are taken from previous models for Aeolian sand transport over fully erodible beds (Carneiro et al., 2011, 2013; Comola et al., 2019). In particular, the elastic constant for normal contact, k_{n}, is estimated using $k_{\mathrm{n}} = \pi d_{\mathrm{m}}Y/4$, where $d_{\mathrm{m}} = 200\,\mu$m is the mean particle size adopted in our simulations, while $Y = 1\,$MPa is the Young's modulus adopted in previous work (Carneiro et al., 2011; Comola et al., 2019) and in our computations. Furthermore, for the elastic constant for tangential constant, we use $k_{\mathrm{t}} = k_{\mathrm{n}}/3$, while the friction coefficient is consistent with values adopted previously (Comola et al., 2019).

Table 1: Parameters of the Discrete-Element-Method.

parameter	symbol	value
elastic constant for normal contact	k_n	$157\,\mathrm{N\,m^{-1}}$
elastic constant for tangential contact	k_t	$52\,\mathrm{N}\,m^{-1}$
viscoelastic damping constant for normal contact	γ_n	$0.2\,\mathrm{kg}\,s^{-1}$
viscoelastic damping constant for tangential contact	γ_t	$0.2\,\mathrm{kg}\,s^{-1}$
Coulomb coefficient of friction	μ_s	0.3
particle diameter	d_i	$[160, 240]\,\mu\mathrm{m}$
particle density	ρ_p	$2650\,\mathrm{kg\,m^{-3}}$

1.4 Numerical implementation and particle-wind coupling

To solve the equations of motion of the granular phase, we employ LAMMPS (Large-scale Atomic/Molecular Massively Parallel Simulator), which is an open source DEM solver based on MPI implementation (Plimpton, 1995). Furthermore, we have extended this solver to incorporate the hydrodynamic description of the turbulent wind flow over the granular surface, developed in previous work (Carneiro et al., 2011; Durán et al., 2012) and briefly reviewed in the main document. To this end, we have included new modules (LAMMPS "fixes") into the granular package of the DEM solver, to set the initial (logarithmic) vertical profile of the mean horizontal wind speed, to compute the drag force, and to update this drag force and the wind profile owing to the process of momentum exchange between the particles and the wind. These modules are available from the corresponding author upon request.

2 Validation of our simulations over fully erodible beds

To verify our numerical simulations, we compare our numerical predictions for the height-integrated mass flux (Q) of wind-blown particles over a fully erodible bed with corresponding wind-tunnel observations of this flux as a function of the wind shear velocity, u_*. We compute Q using the following equation,

$$Q = \frac{\sum_i^N m_i v_i^x}{A} \tag{8}$$

where N is the number of particles in the system, m_i and v_i^x denote the mass and horizontal speed of the $i-$th particle, respectively, and $A = L_x \cdot L_y$ is the horizontal area of the simulation domain. To measure this flux, we start the wind-blown transport process as described in the main document and wait until this transport achieves steady state. The typical (physical) time separating the begin of wind-blown transport from the steady state is about 2-3 seconds and independent of u_* (Carneiro et al., 2011; Durán et al., 2012; Pähtz et al., 2014; Comola et al., 2019). All results reported in the present work refer to the characteristics of steady-state wind-blown transport, and denote mean quantities obtained from averaging over about 5-10 seconds during steady-state transport.

Furthermore, by suitably normalizing the steady-state flux Q, we obtain the following non-dimensional quantity,

$$\hat{Q} = \frac{Q}{\rho_\mathrm{p}\sqrt{(s-1)g d_\mathrm{m}^3}}, \text{ with } s = \frac{\rho_\mathrm{p}}{\rho_\mathrm{f}}, \tag{9}$$

which we plot in Fig. S1 as a function of the Shields number,

$$\Theta = \frac{u_*^2 \rho_\mathrm{f}}{(\rho_\mathrm{p} - \rho_\mathrm{f}) g d_\mathrm{m}} \tag{10}$$

where $\rho_\mathrm{p} = 2650\,\mathrm{kg/m^3}$ and $\rho_\mathrm{f} = 1.225\,\mathrm{kg/m^3}$ denote the densities of the particles and the air, respectively, while $d_\mathrm{m} = 200\,\mu\mathrm{m}$ is the mean particle diameter and $g = 9.81\,\mathrm{m/s^2}$ is gravity.

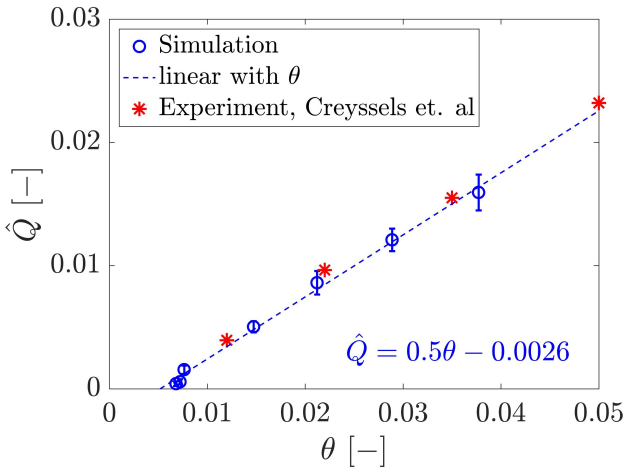

Figure S1: Normalized steady-state flux $\hat{Q}$ as a function of the Shields number Θ, considering a fully erodible bed ($h_\mathrm{mob,0} \approx 15\,d_\mathrm{m}$).

We see in Fig. S1 that our numerical predictions for $\hat{Q}(\Theta)$ (circles) agree quantitatively well with observations from wind-tunnel experiments (Creyssels et al., 2009), denoted by the stars. The best fit to our simulation results using $\hat{Q} = a\Theta + b$ yields $a \approx 0.5$ and $b \approx 0.0026$ (dashed line in Fig. S1), from which obtain the minimal threshold $\Theta_\mathrm{t} \approx 0.0064$ below which no transport occurs ($\hat{Q} = 0$). From Eq. (10), this value of Θ_t leads to the minimal threshold wind shear velocity for sustained transport, $u_{*\mathrm{t}} \approx 0.165\,\mathrm{m/s}$.

We note that the value of $u_{*\mathrm{t}}$ predicted from our simulations is consistent with the prediction that $u_{*\mathrm{t}}$ is about 80% of the minimal threshold wind shear velocity $u_{*\mathrm{ft}}$ required to initiate transport,

$$u_{*\mathrm{ft}} = A_\mathrm{ft}\sqrt{\frac{\rho_\mathrm{p} - \rho_\mathrm{f}}{\rho_\mathrm{f}} g d_\mathrm{m}}, \tag{11}$$

with $A_\mathrm{ft} \approx 0.1$(Bagnold, 1941; Shao & Lu, 2000). Indeed, by applying the mean particle size $d_\mathrm{m} = 200\,\mu\mathrm{m}$ of our simulations in Eq. (11), we obtain $u_{*\mathrm{ft}} \approx 0.206\,\mathrm{m/s}$, i.e., our model is consistent with the relation $u_{*\mathrm{t}} \approx 0.8\,u_{*\mathrm{ft}}$ predicted for wind-blown transport.

3 The modified wind profiles for varying $h_\mathrm{mob,0}$

The initial vertical profile of the horizontal downstream wind velocity u_x is logarithmic and follows Eq. (3) of the main document. However, this wind velocity profile is updated every time-step, since the acceleration of the grains extracts momentum from the air thus creating a negative feedback on the wind. The modification of the wind velocity profile is computed using Eqs. (4) and (5) in the main document. The vertical profiles of the modified wind velocity u_x and the grain-borne shear stress τ_p are shown for different values of the mobile layer thickness $h_\mathrm{mob,0}$ in Fig. S2.

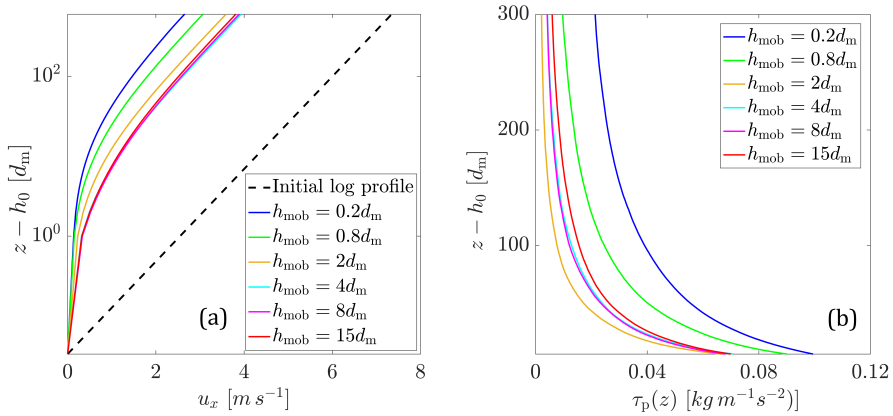

Figure S2: (a) The modified wind profiles for different values of $h_{\mathrm{mob},0}$ alongside the initial logarithmic profile; (b) grain-borne shear stress profile as a function of the height above the bed for different $h_{\mathrm{mob},0}$. The results were obtained with $u_* = 0.30\,\mathrm{m/s}$.

4 Computation of the mean hop length and the mean horizontal impact and lift-off velocities

To compute the mean hop length ℓ_{hop} and the average horizontal impact and lift-off velocities, $u_{0\downarrow}$ and $u_{0\uparrow}$, respectively, we consider only the grains with a minimum vertical lift-off velocity of $\sqrt{6gd}$, i.e., the grains that achieve a minimum height of $3\,d_{\mathrm{m}}$ above the bed height. The values of ℓ_{hop}, $u_{0\downarrow}$ and $u_{0\uparrow}$, are then averaged over a time window of 5 seconds during steady-state sand transport.

The mean horizontal grain velocity or slip velocity u_0 is then computed using

$$u_0 = (u_{0\downarrow} + u_{0\uparrow})/2. \tag{12}$$

Furthermore, to obtain the mean hop length, we start from the mean hop time, which is given by (Ho et al., 2011),

$$t_{\mathrm{hop}} \approx \frac{2v_{0\uparrow}}{g}, \tag{13}$$

where $v_0\uparrow$ is the mean ascending vertical velocity of the grains (also averaged over 5 seconds in the steady state). Furthermore, the horizontal acceleration of the grains is given by,

$$a_{\mathrm{hor}} \approx \frac{(u_{0\downarrow} - u_{0\uparrow})}{t_{\mathrm{hop}}}, \tag{14}$$

so that the mean hop length is approximated as,

$$\ell_{\mathrm{hop}} \approx (u_{0\downarrow} - u_{0\uparrow})\,\frac{v_{0\uparrow}}{g}. \tag{15}$$

5 Relation between the steady-state bed layer thickness, $h_{\mathrm{mob,s}}$, and the initial bed layer thickness, $h_{\mathrm{mob,0}}$

As mentioned in the main document, once the sand transport process begins, the initial thickness of the mobile sand bed applied in the numerical simulations, $h_{\mathrm{mob},0}$, decreases toward a slightly smaller value $h_{\mathrm{mob,s}}$, which is achieved when transport conditions have reached steady state. As depicted in Fig. S3, $h_{\mathrm{mob,s}}$ and $h_{\mathrm{mob},0}$ are linearly related to each

other, and the difference between both values of bed thickness displays a slight increase with u_* owing to the effect of wind shear velocity on enhancing erosion. However, we find that the scaling laws reported in the main document are valid whatever value of bed thickness is chosen, while the following relation applies,

$$\frac{h_{\mathrm{mob,s}}}{d_{\mathrm{m}}} = \left(\frac{h_{\mathrm{mob,0}}}{d_{\mathrm{m}}} - C_{\mathrm{b}}\frac{u_*}{\sqrt{g d_{\mathrm{m}}}}\right)\cdot \Theta\left(\frac{h_{\mathrm{mob,0}}}{d_{\mathrm{m}}} - C_{\mathrm{b}}\frac{u_*}{\sqrt{g d_{\mathrm{m}}}}\right) \tag{16}$$

where $C_{\mathrm{b}} \approx 0.02$ is an empirical parameter and $\Theta(x)$ denotes the Heaviside function, i.e., $\Theta(x) = 1$ if $x \geq 0$ and $\Theta(x) = 0$ if $x < 0$. Therefore, the term $C_{\mathrm{b}} u_*/(\sqrt{g d_{\mathrm{m}}})$ in Eq. (16) denotes the thickness of the total eroded layer, relative to the particle size, from the beginning of transport until steady state (i.e., as the bed thickness evolves from $h_{\mathrm{mob,0}}$ toward $h_{\mathrm{mob,s}}$).

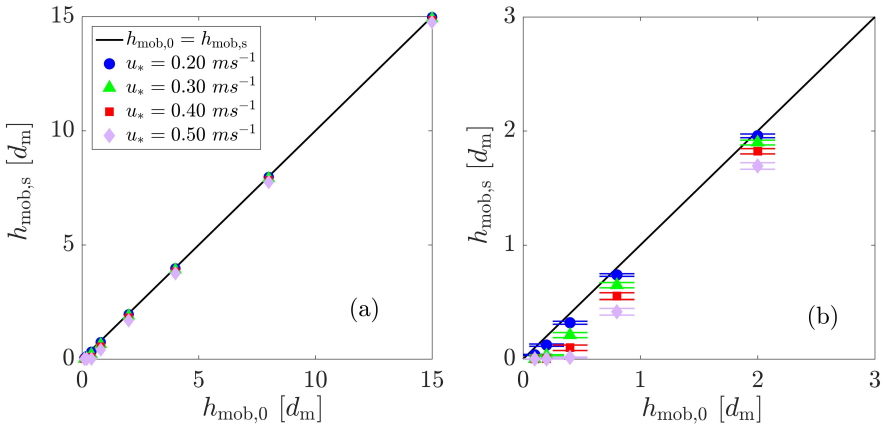

Figure S3: (a) Values of the bed layer thickness at steady-state transport, $h_{\mathrm{mob,s}}$, plotted against the initial values of bed layer thickness, $h_{\mathrm{mob,0}}$, for different values of the wind shear velocity u_*. The plot in (b) denotes a zoom into the region of bed layer thickness comparable to the particle size.

In particular, by virtue of Eq. (16), we can express the coefficient b in Eq. (7) of the main document as a function of $h_{\mathrm{mob,s}}$ approximately as

$$b \approx k_{\mathrm{s}}\left(\frac{h_{\mathrm{mob,s}}}{d_{\mathrm{m}}} + C_{\mathrm{b}}\frac{u_*}{\sqrt{g d}} - c_{\mathrm{s}}\right)^{-1} \tag{17}$$

which yields $k_{\mathrm{s}} \approx 0.25$ and $c_{\mathrm{s}} \approx 0.15$ from the best fit to the simulation data (Fig. S4).

6 Transport layer thickness as a function of $h_{\mathrm{mob,0}}$

As explained in the main document, the transport layer expands gradually as the soil erodibility conditions change from fully erodible to rigid. To quantify this process, we compute the characteristic length-scale l_ν associated with the nearly exponential decay of the particle concentration $\nu(z)$ with the height z above the ground, i.e.,

$$\nu(z) = \nu_0 \exp(-z/l_\nu) \tag{18}$$

where ν_0 is the particle concentration extrapolated to the bed ($z = 0$). Fig. S5 shows the behavior of l_ν as a function of the thickness of mobile sand layer on the ground, $h_{\mathrm{mob,0}}$. We see that, when the rigid ground is flat, l_ν decreases monotonically as $h_{\mathrm{mob,0}}$ increases toward

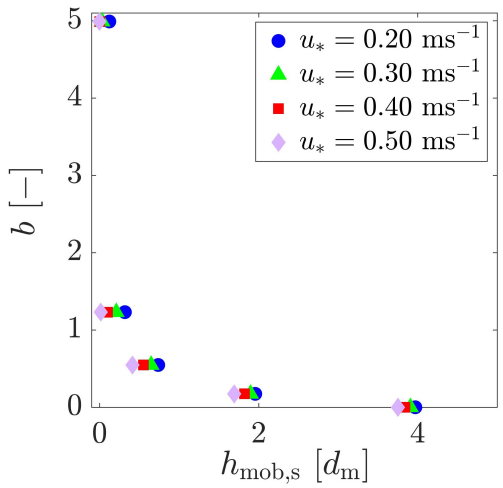

Figure S4: The plot shows the values of the parameter b in Eq. (7) of the main document, obtained from the best fit to the simulation data as a function of $h_{\mathrm{mob,s}}$, for different values of the wind shear velocity u_*.

$15\,d_{\mathrm{m}}$ (the fully erodible bed scenario). However, when the rigid surface is armoured with non-erodible elements (which in our simulations have the same size as the mobile particles), a minimum in l_ν is observed near $h_{\mathrm{mob},0} = 2\,d_{\mathrm{m}}$. This minimum can be explained by the prevailing occurrence of backward ejecta in the range $h_{\mathrm{mob},0} \lesssim 2\,d_{\mathrm{m}}$ (as described in the main document), which leads to lower values of l_ν in this range when non-erodible particles cover the ground, compared to the flat ground scenario. As $h_{\mathrm{mob},0}$ becomes much larger than the particle size, the effect of the immobile particles on the Aeolian transport thickness becomes negligible, and l_ν approaches asymptotically the value corresponding to the fully erodible bed as shown in Fig. S5.

Acknowledgments

The data for validation with experiments in Fig. S1 is available from (Creyssels et al., 2009), and the rest is made available online (https://doi.org/10.6084/m9.figshare.17942519). We thank the German Research Foundation (DFG) for funding through the Heisenberg Programme and the grant - 348617785.

References

Bagnold, R. A. (1941). *The physics of blown sand and desert dunes.* Methuen, London.

Brilliantov, N. V., Spahn, F., Hertzsch, J.-M., & Pöschel, T. (1996). Model for collisions in granular gases. *Physical review E*, *53*(5), 5382. doi: https://doi.org/10.1103/PhysRevE.53.5382

Carneiro, M. V., Araújo, N. A. M., Pähtz, T., & Herrmann, H. J. (2013). Midair collisions enhance saltation. *Physical review letters*, *111*(5), 058001. doi: https://doi.org/10.1103/PhysRevLett.111.058001

Carneiro, M. V., Pähtz, T., & Herrmann, H. J. (2011). Jump at the onset of saltation. *Physical Review Letters*, *107*(9), 098001. doi: https://doi.org/10.1103/PhysRevLett.107.098001

Comola, F., Gaume, J., Kok, J., & Lehning, M. (2019). Cohesion-induced enhancement of aeolian saltation. *Geophysical Research Letters*, *46*(10), 5566–5574. doi: https://doi.org/10.1029/2019GL082195

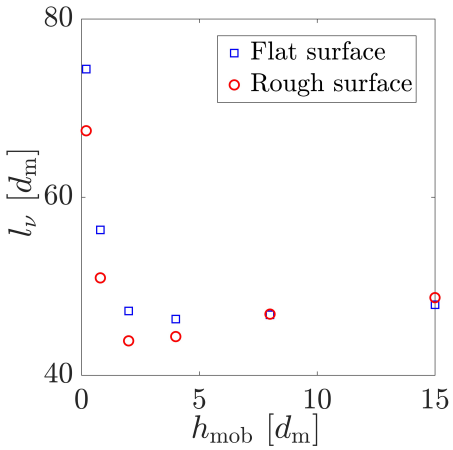

Figure S5: Thickness l_ν of the transport layer as a function of the thickness $h_{\mathrm{mob},0}$ of the mobile sediment layer covering the non-erodible surface, which consists of a flat horizontal surface (blue symbols) and a sheet of immobile particles (red symbols). The results were obtained with $u_* = 0.30\,\mathrm{m/s}$.

Creyssels, M., Dupont, P., El Moctar, A. O., Valance, A., Cantat, I., Jenkins, J. T., ... Rasmussen, K. R. (2009). Saltating particles in a turbulent boundary layer: experiment and theory. *J. Fluid Mechanics*, *625*, 47. doi: https://doi.org/10.1017/S0022112008005491

Cundall, P. A., & Strack, O. D. (1979). A discrete numerical model for granular assemblies. *geotechnique*, *29*(1), 47–65. doi: https://doi.org/10.1680/geot.1979.29.1.47

Di Renzo, A., & Di Maio, F. P. (2004). Comparison of contact-force models for the simulation of collisions in dem-based granular flow codes. *Chemical Engineering Science*, *59*(3), 525-541. doi: https://doi.org/10.1016/j.ces.2003.09.037

Durán, O., Andreotti, B., & Claudin, P. (2012). Numerical simulation of turbulent sediment transport, from bed load to saltation. *Physics of Fluids*, *24*(10), 103306. doi: https://doi.org/10.1063/1.4757662

Fan, F., Parteli, E. J. R., & Pöschel, T. (2017). Origin of granular capillarity revealed by particle-based simulations. *Phys. Rev. Lett.*, *118*, 218001. doi: https://doi.org/10.1103/PhysRevLett.118.218001

Ho, T. D., Valance, A., Dupont, P., & El Moctar, A. O. (2011). Scaling laws in aeolian sand transport. *Physical Review Letters*, *106*(9), 094501. doi: https://doi.org/10.1103/PhysRevLett.106.094501

Kruggel-Emden, H., Simsek, E., Rickelt, S., Wirtz, S., & Scherer, V. (2007). Review and extension of normal force models for the discrete element method. *Powder Technol.*, *171*, 157-173. doi: https://doi.org/10.1016/j.powtec.2006.10.004

Luding, S. (2008). Cohesive, frictional powders: contact models for tension. *Granular matter*, *10*(4), 235. doi: https://doi.org/10.1007/s10035-008-0099-x

Machado, M., Moreira, P., Flores, P., & Lankarani, H. M. (2012). Compliant contact force models in multibody dynamics: Evolution of the hertz contact theory. *Mechanism and Machine Theory*, *53*, 99-121. doi: https://doi.org/10.1016/j.mechmachtheory.2012.02.010

Pähtz, T., Parteli, E. J. R., Kok, J. F., & Herrmann, H. J. (2014). Analytical model for flux saturation in sediment transport. *Physical Review E*, *89*(5), 052213. doi: https://doi.org/10.1103/PhysRevE.89.052213

Parteli, E. J. R., Schmidt, J., Blümel, C., Wirth, K.-E., Peukert, W., & Pöschel, T. (2014). Attractive particle interaction forces and packing density of fine glass powders. *Sci.*

Rep., *4*, 6227. doi: https://doi.org/10.1038/srep06227

Plimpton, S. (1995). Fast parallel algorithms for short-range molecular dynamics. *Journal of computational physics*, *117*(1), 1–19. (Website of the DEM solver LAMMPS: `https://lammps.sandia.gov/`) doi: https://doi.org/10.1006/jcph.1995.1039

Pöschel, T., & Schwager, T. (2005). *Computational granular dynamics.* Springer Berlin Heidelberg. doi: https://doi.org/10.1007/3-540-27720-X

Santos, A. P., Bolintineanu, D. S., Grest, G. S., Lechman, J. B., Plimpton, S. J., Srivastava, I., & Silbert, L. E. (2020). Granular packings with sliding, rolling, and twisting friction. *Phys. Rev. E*, *102*, 032903. doi: https://doi.org/10.1103/PhysRevE.102.032903

Schäfer, J., Dippel, S., & Wolf, D. E. (1996). Force Schemes in Simulations of Granular Materials. *J. Phys. I France*, *6*, 5-20. doi: https://doi.org/10.1051/jp1:1996129

Schmidt, J., Parteli, E. J., Uhlmann, N., Wörlein, N., Wirth, K.-E., Pöschel, T., & Peukert, W. (2020). Packings of micron-sized spherical particles: Insights from bulk density determination, x-ray microtomography and discrete element simulations. *Advanced Powder Technology*, *31*(6), 2293-2304. doi: https://doi.org/10.1016/j.apt.2020.03.018

Shao, Y., & Lu, H. (2000). A simple expression for wind erosion threshold friction velocity. *Journal of Geophysical Research: Atmospheres*, *105*(D17), 22437-22443. doi: https://doi.org/10.1029/2000JD900304

Silbert, L. E., Ertaş, D., Grest, G. S., Halsey, T. C., Levine, D., & Plimpton, S. J. (2001). Granular flow down an inclined plane: Bagnold scaling and rheology. *Physical Review E*, *64*(5), 051302. doi: https://doi.org/10.1103/PhysRevE.64.051302

Verbücheln, F., Parteli, E. J. R., & Pöschel, T. (2015). Helical inner-wall texture prevents jamming in granular pipe flows. *Soft Matter*, *11*(21), 4295–4305. doi: https://doi.org/10.1039/c5sm00760g